Chemo-physico-mechanical properties of the interface zone between bacterial PLA self-healing capsules and cement paste

Cement and Concrete Research 138 (2020) 106228

Contents lists available at ScienceDirect

Cement and Concrete Research

journal homepage: www.elsevier.com/locate/cemconres

Chemo-physico-mechanical properties of the interface zone between bacterial PLA self-healing capsules and cement paste

C. Romero Rodríguez[a,*], F. França de Mendonça Filho[a], L. Mercuri[a,b], Y. Gan[a], E. Rossi[a], G. Anglani[b,c], P. Antonaci[b,c], E. Schlangen[a], B. Šavija[a]

[a] Microlab, Department of 3MD, Faculty of Civil Engineering and Geosciences, Delft University of Technology, Stevinweg 1, 2628CN Delft, the Netherlands
[b] Department of Structural, Geotechnical and Building Engineering, Politecnico di Torino, Corso Duca degli Abruzzi 24, 10129 Turin, Italy
[c] Responsible Risk Resilience Centre, Politecnico di Torino, Viale Mattioli 39, 10125 Torino, Italy

ARTICLE INFO

Keywords:
Bacterial self-healing concrete
Micromechanics
Nanoindentation
Poly-lactic acid capsules
Lattice model

ABSTRACT

In this study, the interface between different types of bacteria-embedded self-healing polylactic acid capsules (PLA) and cement paste is investigated. Particularly, the changes in microstructure and mechanical properties of the interface with respect to bulk cement paste were studied. First, nanoindentation was performed to obtain maps of hardness and elastic modulus in the interfaces. Lattice modeling of uniaxial tensile test on the mapped locations was performed then to obtain the overall tensile strength and stiffness of the interface. Moreover, hydrates assemblage and chemical composition around the PLA particles were studied through Backscattering Electron images and Energy Dispersive X-ray Spectroscopy. The ratios between resulting tensile strength and elastic modulus of the interface with respect to bulk paste were obtained for each PLA type. The results suggest that PLA can be tailored to optimize the physico-mechanical properties of the interface and hence, the mechanical behavior and triggering efficiency of the self-healing system.

1. Introduction

Autonomous self-healing (SH) of cracks in concrete is a smart solution to boost the durability of cement-based materials. A key feature of an autonomous system is the way that SH is triggered, which is closely linked to how the healing agents are incorporated into the composite. To this purpose, the healing agents are either specifically placed in prone to crack zones of the structural element (i.e. vascular systems) [1] or randomly distributed in the cement matrix, i.e. capsules [2–4], (coated) fibres [5], where the inclusions themselves steer the crack patterns. In the latter case, mechanical triggering should be such that the overall mechanical performance of the SH composite approaches the one of the non-SH material.

Although a huge variety of engineered SH systems for concrete have been developed in the past decades [6], there seems to be a tendency to favour encapsulation as triggering mechanism [7–9]. One such example is the introduction of bacteria spores and nutrients embedded in capsule-like particles [10–14]. Encapsulation of bacterial spores is needed not only as a mechanical triggering mechanism but also to protect the alkaliphilic bacterial spores during mixing of concrete, to prevent their germination prior to cracking and to contain calcium sources and activation nutrients so necessary for their metabolic activity [15,16]. Previous research on the use of bacteria-embedded poly-lactic-acid (PLA) capsules as healing agent has proven its potential to satisfy both mechanical and functional requirements of the resulting SH system [17]. The main advantage of the use of PLA as carrier for the healing agents is that its metabolic conversion by the bacteria leads to the production of CO2, which in turns results in more crack carbonation in presence of calcium cations. Since a carbon source is a mandatory inclusion in this self-healing system regardless of the carrier, the use of PLA as encapsulating matrix reduces the volume of healing particles added into concrete in order to obtain the same healing capacity [17]. Nevertheless, the biodegradable PLA partially hydrolyses in alkaline environments ultimately affecting hydration kinetics of the cement paste [18]. To what degree and extent the hydration reaction around the PLA particle is modified depends on the PLA type and should be investigated case by case. From previous studies [2,18], it can be hypothesized that an interface zone (IZ) can be located around the PLA particle, presenting different hydration degree in comparison to the bulk paste. As a consequence modified mechanical properties of the interface zone (IZ) are expected, as well as a different mechanical behavior of the overall SH composite.

Despite the need for the capsules to be able to steer the crack propagation and make the healing agents available at the crack location, an

* Corresponding author.
E-mail address: c.romerorodriguez@tudelft.nl (C.R. Rodríguez).

https://doi.org/10.1016/j.cemconres.2020.106228
Received 25 May 2020; Received in revised form 3 September 2020; Accepted 12 September 2020

important requirement for SH systems is that the additives should not excessively weaken the resulting composite. In the case of PLA capsules, the thickness and mechanical properties of the IZ may have a non-negligible influence on the fracture behavior of the self-healing system due to the microstructural changes that alterations in hydration degree may yield. Hilloulin et al. [19] verified that bond strength between PLA capsules and cement matrix is relatively low (about one third of typical tensile strengths of cement paste and one sixtieth of PLA), therefore debonding is more likely to occur than capsule fracture. These findings confirm that quantifying the interface mechanical properties is relevant to design a SH material that is tough and at the same time capable of being mechanically triggered. Furthermore, the mechanical properties of the IZ can be used as input for modeling fracture of the SH system at the mesoscale [20]. Moreover, by changing a wide range of parameters, optimization of relevant material properties can be performed via numerical simulations [21]. The proposed approach may result in higher accuracy for optimization of SH systems than non-experimentally informed approaches [22] or stereological approaches [23,24].

In this study we aim to quantify the tensile strength and elastic modulus of the IZ around PLA capsules, for their eventual use as input for mesoscale simulations of the SH composite. First, mapping of the elastic modulus and the hardness of the IZ around different types of bacteria-embedded PLA particles, inside cement paste, was done through grid nanoindentation. Also the bulk unaffected cement paste was tested as reference. A similar methodology was proposed in [25] to study the interface of cement-based repair systems. The nanoindentation mappings were then used as input to simulate uniaxial tensile tests through lattice fracture model. Moreover, Scanning Electron Microscopy in Backscattering Electron and Energy Dispersive X-ray Spectroscopy modes (SEM/BSE/EDS) was performed to study the hydrates assemblage distribution and chemical composition around the PLA particles. The former allowed determining the extension of the IZ to calculate the stiffness, whereas the latter allowed to explain the possible causes of the observed variation in mechanical properties. The resulting tensile strength and elastic modulus of the IZ were compared to the values simulated for the reference cement paste and their ratios were obtained for each PLA type.

2. Experimental methodology

2.1. Materials and mixtures

Cement paste samples were produced with cement CEM I 52.5R from ENCI Netherlands, tap water and three different types of self-healing bio-polymeric particles, supplied by Basilisk (the Netherlands). All self-healing particle types were composed of a poly-lactic acid derivate matrix (PLA), embedded bacterial spores of Bacillus cohnii-related strains and growth-required nutrient inorganic salts [26]. The three types of particles differed in their production process and resulting shape, while polymer composition and dosage of nutrients and bacterial spores were the same, according to the producers. Approximate main composition of the PLA capsules can be found in Table 1 [26]. For the sake of nomenclature herein we refer to the different particles as PLA-I (irregular), PLA-II (spherical) and PLA-III (lamellar) (see Fig. 1). Their density was measured as 1200 kg/m^3. The particle sizes were between 0.5 and 1 mm. By means of the Sauter mean diameter, measured by laser diffraction, the resulting specific surface area of particles PLA-I, -II and -III resulted 7.75×10^{-5}, 1.11×10^{-5} and 15.6×10^{-5} cm^2/g [27]. The chemical composition of the cement is reported in Table 2.

Table 1
General composition of bacterial PLA self-healing capsules.

Ingredient	Weight percentage of product
PLA	50 − 80
Bacterial spores	0.1 − 2
Nutrients	10.5 − 43
Water	1 − 5

Four different cement pastes were designed with water-to-cement ratio (w/c) of 0.45. A mixture containing no healing particles was prepared as reference, herein referred to as CP. The other mixtures contained a certain particle type (I, II or III) with dosage of 0.6 % by weight of cement, which corresponds to 0.4 % by volume of composite. This content was chosen in order to isolate the influence of each single particle from each other on the surrounding cement paste. The investigated mixtures will be hereafter referred to as SH-I, SH-II and SH-III for pastes with capsules of PLA-I, -II and -III, respectively.

A Hobart planetary mixer was used to prepare the fresh pastes. All dry components were mixed first for 1 min at low speed. Water was added into the running mixer in the following 30 s and the components were left to mix for extra 30 s. Afterwards, the walls of the mixer were scraped and mixing was continued for 1 min and 30 s at low speed and 30 s at medium speed. The pastes were poured into plastic vessels with a diameter of 35 mm and a height of 70 mm. The samples were then sealed with plastic sheet and left to harden for 24 h at laboratory conditions. Afterwards the samples were demoulded and stored in a fog chamber with temperature and relative humidity set at 20 °C and 95 %, respectively until the age of 28 days.

2.2. Isothermal calorimetry

To determine the effect of PLA particles on the cement hydration, the heat released during the first 120 h of hydration was monitored by means of an eight-channel isothermal calorimeter (TAM Air 3114/3236, Thermometric AB, Sollentuna, Sweden), operating at 600 mW and 20 °C. For this test, a different dosage of PLA particles was selected, namely 1.3 % by weight of cement. Such choice was made in accordance with literature studied reporting on the dosage optimization for self-healing functionality [28]. The total weight of the self-healing pastes tested was of 7.565 g, whereas for the reference paste the weight was 7.25 g. Two duplicate tests were performed for each mixture.

2.3. Sample preparation

At the end of the curing period of 28 days, the cylindrical samples were sawn into 3–5 mm thick slices and further cut into rectangular sections with dimensions 10 × 10 mm^2. Selected slices, containing 1 to 3 (far apart) particles, were immersed in isopropanol for approximately 7 days and further dried in an oven at 40 °C for 10 min. The sections were put in a desiccator for at least 24 h. This procedure was performed to stop hydration and to dry the samples prior to preparation for the nanoindentation procedure. At the end, one section per mixture was used for subsequent measurements. The resulting sections were first ground with silicon carbide paper with a mesh grade of 1200 at 150 RPM and later polished with diamond paste (Struers) with grain sizes 9, 6, 3, 1 and 1/4 μm for 15, 15, 30 and 30 min, respectively, also at 150 RPM. After each respective step, the sections were put in an ethanol bath within an ultra-sonicator for 5 min in order to remove diamond particles and were further rinsed with ethanol prior to the next polishing step.

2.4. Nanoindentation

Nano Indenter (G200, KLA, USA) with a diamond Berkovich tip was used to perform grid nanoindentation on the prepared sections at 6 different locations per paste type. In the case of SH sections, for each location a grid of 5 × 15 indents, with a spacing of 10 μm in both directions, was performed to map hardness (H) and elastic modulus (E). The orientation of the grid was such that its short side was parallel to the boundary of the PLA particle and its origin was right at the

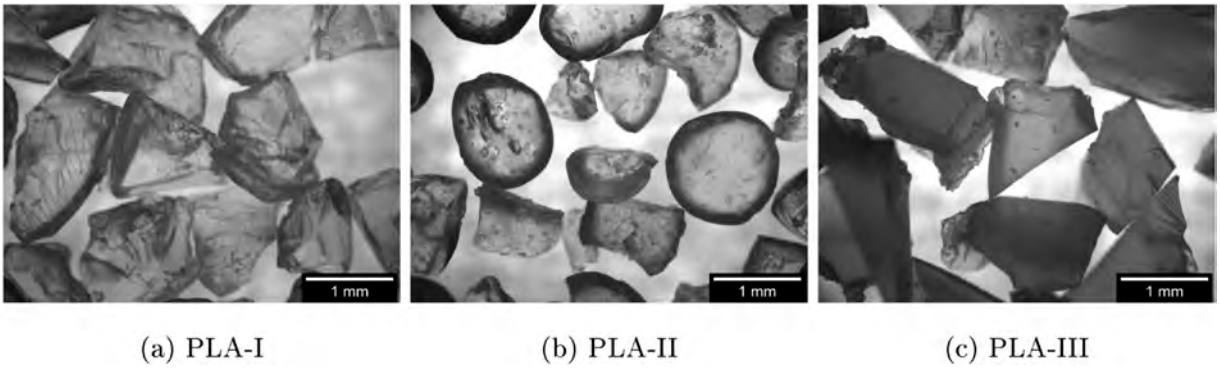

Fig. 1. Bacteria-embedded PLA capsules used in this work.

Table 2
Chemical composition of CEM I 52.5R in [%] measured through XRF.

CaO	SiO_2	Al_2O_3	Fe_2O_3	K_2O	TiO_2	Other
68.7	17.4	4.1	2.8	0.6	0.3	6.1

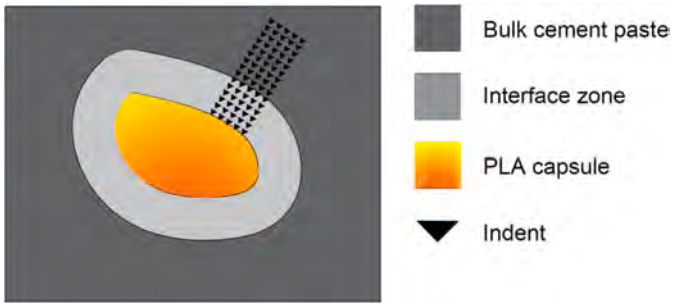

Fig. 2. Schematics of grid nanoindentation in IZ of self-healing paste sections.

boundary. In the case of mixture CP, the grid consisted of 5 × 10 indents with same spacing as the SH pastes. No preferred location or orientation was pursued for the latter. The schematics of the grid positioning within the interface are shown in Fig. 2.

Using the continuous stiffness measurement (CSM) developed by Oliver and Pharr [29], E and H were obtained as a continuous function of the depth of penetration of the indenter. To ensure the accuracy of measurements, a standard quartz was used for the calibration of the indenter tip before each test. The surface approach velocity was 10 nm/s while the strain rate in the material was kept as 1/s. The maximum indentation depth was fixed at 1000 nm. A Poisson ratio of 0.2 was assumed for the calculation of E. The average elastic modulus and hardness were calculated in the displacement range between 500 and 650 nm to avoid the scatter of lower indentation depths where surface roughness may lead to erroneous results.

2.5. Scanning Electron Microscopy and image analysis

After nanoindentation, the same sections were coated with a thin layer of gold (10 nm) to ensure good surface conductivity. Scanning Electron Microscopy (SEM) in Back Scattered Electrons (BSE) mode was performed on the pastes in order to investigate the extension of the interface zones surrounding the different PLA particles. Furthermore, Energy Dispersive X-ray Spectroscopy (EDS) was performed to investigate the variation of elemental composition at the interface zones with respect to that of the bulk cement paste. An Environmental Scanning Electron Microscope (ESEM XL30, FEI, Thermo Fisher Scientific) was used at high vacuum for the acquisition of the micrographs.

For the BSE analysis, the instrument was operated with accelerating voltage of 20 kV and at a working distance of 10 mm. A magnification of 500× was employed for all SH sections, while a magnification of 550× had to be used for CP sections. The resolution of the images was 0.123 µm. Since it was of interest to investigate the interface zone, micrographs were acquired at locations where the boundary between PLA particle and surrounding cement paste was present. For statistical relevance 30 locations were randomly chosen and two contiguous micrographs per location were acquired. The obtained 16-bit BSE images, taken at contiguous locations, were stitched through the freeware ImageJ [30]. The machine learning tool Trainable Weka Segmentation (TWS) [31] (within the same software) was used to segment anhydrous cement grains. Global thresholding was used to segment the resolved porosity.

For the EDS analysis the accelerating voltage was set at 15 kV. The detector was a SUTW (sapphire) with a calibrated resolution of 132 eV and deadtime of around 10 %. The take-off angle was 35.3° and sample to detector distance was 10 mm. Prior to the acquisition of the spectra, the beam current was measured using a Faraday cup and a picoammeter. Per each batch type, 3 interface locations (among the ones used for BSE analysis) and 3 locations far from the particles (representative of the bulk paste) were chosen to perform point analysis. Ten points were chosen semi-randomly per analysis to exclude anhydrous cement grains and pores. The locations for the points in the interfaces were within 30 µm from the PLA particle boundary. After acquisition, standards based correction was performed previous to the quantification of mass and atomic percentage using the NIST DTSA-II software [32]. The mineral standards used for such corrections are shown in Table 3.

3. Lattice fracture modeling

Grid nanoindentation mapping, as performed in this study, cannot lead to conclusions regarding the overall mechanical performance of the material. Hydrated cement paste is highly heterogeneous and

Table 3
Standards used for EDS quantification.

Element	Symbol	Mineral used for correction	Chemical composition
Sodium	Na	Albite	$NaAlSi_3O_8$
Magnesium	Mg	Periclase	MgO
Aluminum	Al	Jadeite	$NaAlSi_2O_6$
Silicon	Si	Quartz	SiO_2
Phosphorus	P	Apatite	$Ca_5P_5O_{12}F$
Sulfur	S	Anhydrite	$CaSO_4$
Chlorine	Cl	Tugtupite	$Na_4AlBeSi_4O_{12}Cl$
Potassium	K	Sanidine	$KAlSi_3O_8$
Calcium	Ca	Calcite	$CaCO_3$
Iron	Fe	Haematite	Fe_2O_3
Zinc	Zn	Willemite	Zn_2SiO_4
Oxygen	O	Oxygen determined by stoichiometry	

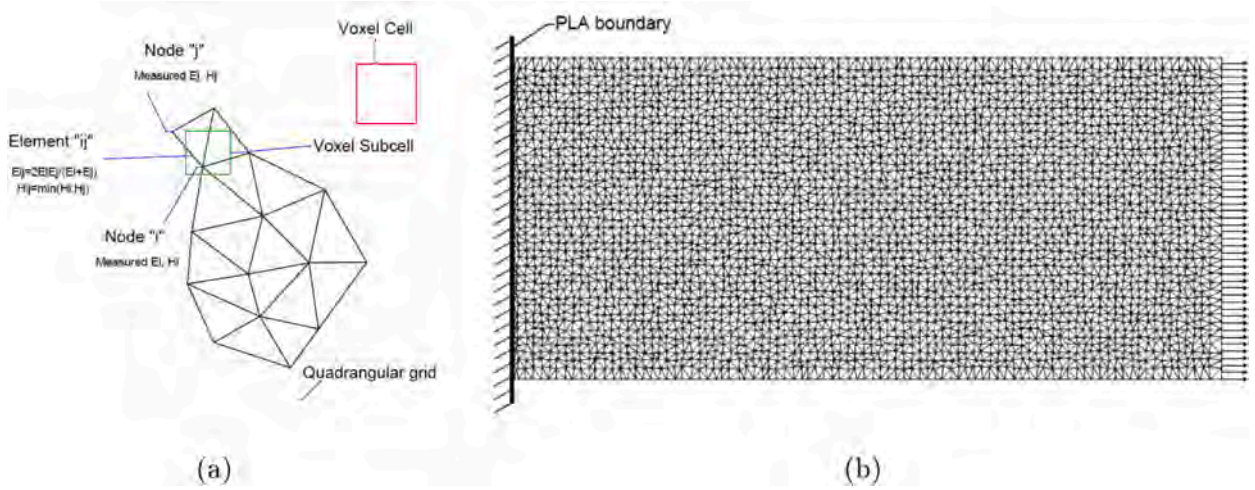

Fig. 3. Lattice model discretization procedure a) and simulated loading condition in uniaxial tensile mode b).

within each defined phase, micromechanical properties vary depending on many factors (i.e. w/c ratio, curing temperature, cement composition, etc. [33]). An approach to understand the composite mechanical behavior is to use the output of appropriately designed grid nanoindentation, at several locations, as input for numerical fracture models [34,35]. The chosen model should allow for imposition of local mechanical properties (measured through grid nanoindentation) in order to account for the heterogeneity of the cement paste. An increasingly popular choice to simulate fracture of heterogeneous brittle materials is lattice models [36,37]. This type of models consists in an assembly of discrete two-nodes elements (lattice beams) that represents a continuum. For the discretization of the domain, the nodes are placed pseudo-randomly inside each cubic cell of a quadrangular grid. The ratio between the specified sub-cell and the cubic cell dimensions determines the randomness of the set of nodes. Subsequently, a Voronoi tessellation is performed with respect to the previously placed nodes in the domain. Nodes belonging to adjacent Voronoi cells are joined by lattice beams. A schematic representation of the above mentioned procedure is reported in Fig. 3a. Commonly, the elements are assigned a linear-elastic constitutive law, characterized by inputs such as elastic and shear moduli, tensile and compressive strengths [38]. It is also possible to assign non-linear constitutive laws [39].

In this work we used the earlier simplification, as the use of linear-elastic elements also leads to a sufficiently accurate simulation of post-peak softening and ductility of the material. The linear-elastic properties of each element were assigned the corresponding values obtained from grid nanoindentation. In a previous study [25] the authors suggested a mesh size below 1.75 μm for microstructure scale simulations. Herein we used 1 μm as cell size with a randomness of 0.2 for the positioning of the nodes. For assigning the elemental properties we first proceeded to linearly interpolate the grid nanoindentation elastic moduli and hardness values in the new grid nodes. Afterwards, for each lattice element with nodes i and j, the elastic modulus (E_{ij}) was calculated as if the element was composed of two springs in parallel with moduli E_i and E_j, respectively [40]:

$$\frac{2}{E_{ij}} = \frac{1}{E_i} + \frac{1}{E_j} \tag{1}$$

Consequently, the shear modulus of the element (G_{ij}) was obtained through Eq. 2. A Poisson ratio (ν) of 0.2 was used.

$$G_{ij} = \frac{E_{ij}}{2(1+\nu)} \tag{2}$$

The ratio between measured hardness and tensile strength ($f_{t,\ ij}$) used was taken as 12, as suggested in [41] and further confirmed in [42]. The elemental tensile strength was then calculated as suggested in [40]:

$$f_{t,ij} = \min(f_{t,i}; f_{t,j}) \tag{3}$$

The compressive strength ($f_{c,\ ij}$) to tensile strength ratio was taken as 10 which has been experimentally confirmed for such length scales in [43].

After discretization and assignment of input properties, lattice fracture model was used to simulate uniaxial tensile test on the 2D meshes. The tensile test was simulated on the PLA-pastes by blocking all degrees of freedom on the origin of the IZ (at the boundary with the PLA particle) and by imposing a unitary displacement on the opposite side. Same boundary conditions were used for the simulations on the bulk cement paste but the choice of the side for null degrees of freedom was done arbitrarily. Typical uniaxial tensile configurations for PLA-pastes and bulk CP meshes are shown in Fig. 3b.

4. Results

4.1. Kinetics of hydration of cement paste with PLA particles

In a previous work [18], it was observed that similar PLA capsules, as in this study, interfered in the hydration of cement paste. According to a study of [44], organic PLA undergoes alkaline degradation into molecules containing α-hydroxy carboxyl group which can be very absorbing and therefore retarding. Notwithstanding, much contradictory discussions can be found in literature regarding the effects of PLA on hydration kinetics [45,46]. Some studies report acceleration and other, retardation. Therefore it results relevant to understand how and to what extent the studied PLA particles modify the hydration kinetics of the surrounding paste when compared to a reference containing no PLA capsules (Fig. 4). The reported curves correspond to one of the test duplicates for each mixture as no relevant differences were found among replicates.

As can be observed in Fig. 4a, the induction period is slightly prolonged for SH-I and SH-II of about 60 and 20 min, respectively. In the case of SH-III the induction period occurs 17 h later than the reference paste and takes up considerably more energy. Since induction period seems to be associated most likely to ionic concentration in the solution [47], this may suggest that dissolution of PLA/nutrients is causing the retardations. As for the differences between the PLA capsule types, shape seems to be the only differing factor with resulting surface areas as follows PLA-II < PLA-I < PLA-III. Furthermore, production processes may have affected the solubility of the bio-polymer.

Acceleration of hydration occurs at a similar rate as the reference

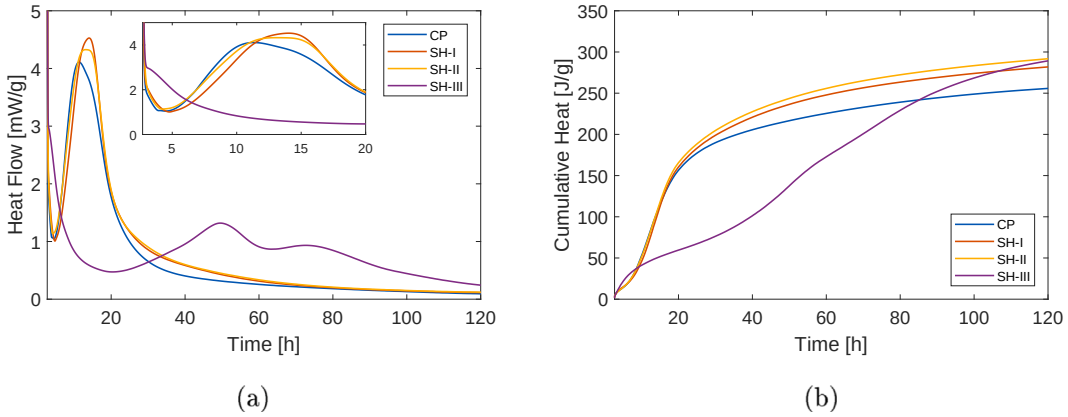

Fig. 4. Heat flow a) and cumulative heat b) of the studied hydrating cement pastes CP, SH-I, SH-II and SH-III from first 3 to 120 h of hydration.

for SH-I and SH-II, yet the maximum of the heat flow is higher for II and I, respectively. Furthermore SH-II presents a flatter peak than SH-I and the reference. The acceleration rate of SH-III is quite lower than CP and the peak is delayed 35 h with respect to the reference, denoting very slow nucleation of hydrates on the cement grain surfaces. Moreover the peak heat flow is 4 times lower than the reference. A possible explanation for the behavior of SH-III is still the low dissolution rate of cement grains, which cannot compensate timely for the nucleation and growth of hydrates.

At the onset of the respective deceleration periods the cumulative heat of hydration for the studied pastes had the following trend: SH-III < CP < SH-I < SH-II. After the primary acceleration peak, SH-III presented a secondary peak (or broad shoulder) in the heat flow curve. Further studies should be carried out to understand what the cause of this anomaly is.

To summarize, while PLA-I and PLA-II provoke moderate changes in the cement hydration kinetics, PLA-III seems to dramatically affect cement hydration in the first 120 h.

4.2. Chemical and physical properties of the interface zone

4.2.1. Degree of hydration and porosity

In Fig. 5, an example of the SEM/BSE gray-valued (GV) micrograph of the interface zone of SH-III is reported, as well as the resulting segmentation of the anhydrous (red) and hydrates (green and purple) phases through TWS in b) and the segmentation of pores (in white) through thresholding in c). By defining the position 0 of the IZ as the particle-paste boundary, a MATLAB code was developed and used to shift all pixel rows to start at such position 0, making possible the calculation of the degrees of hydration and porosity at different distances from position 0.

The degree of hydration (α) was estimated according to Powers & Brownyard [48] assumption that the volumetric fraction of hydration products (F_{hp}) is 2.1 times that of their originating unhydrated grains (F_{up}) through:

$$\alpha = \frac{F_{hp}/2.1}{F_{hp}/2.1 + F_{uc}} \quad (4)$$

The linear-traverse and point counting methodology [49] was employed to assess the volumetric ratios of F_{hp} and F_{up}. Linear-traverses were chosen in correspondence of every pixel column of the segmented images. Hydration products and anhydrous grains pixels alike were counted and the degree of hydration and porosity were computed per linear-traverse.

The graphs shown in Fig. 6 report the degrees of hydration and porosity profiles along the direction perpendicular to the PLA boundary in SH-I, -II and -III, in order to define the extension of their respective interface zones. The error bars represent the standard deviation among

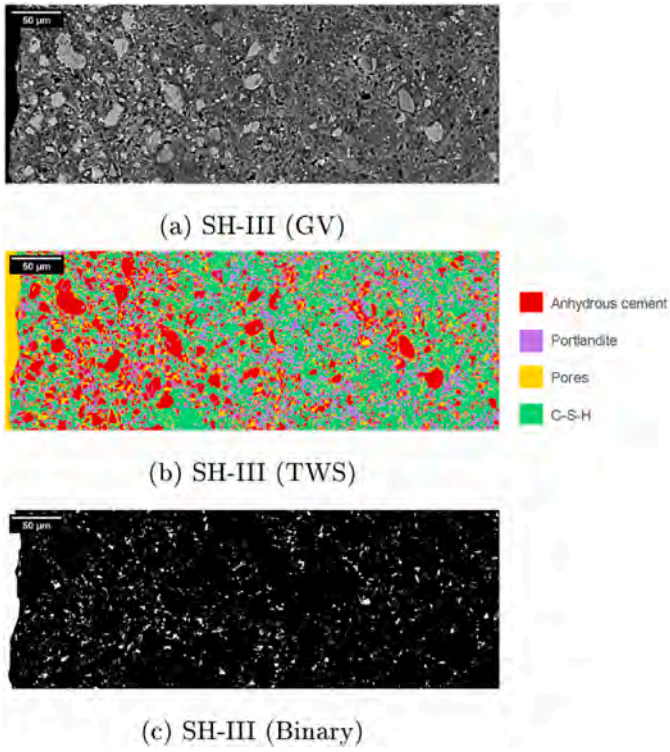

Fig. 5. BSE image of the interface zone of SH-III (PLA particle at the left) in Gray-Value a), after Trainable Weka Segmentation b) and after pore thresholding c).

the different micrographs for each position. The limit values for the bulk zone, obtained from CP micrographs, are reported in each graph in relation to degree of hydration or porosity. In this regard it is worth mentioning that due to the different magnification used to image CP bulk zones (550×), values cannot be rigorously compared. A higher resolution image will yield better defined boundaries of the phases and more accurate quantification of their area, whereas the opposite applies to lower magnifications. This applies specially to small phases (like pores) where the surface to volume ratio is higher.

From the profiles of porosity no clear trend could be found. This is somewhat logical since all the porosity cannot be resolved at these magnifications. The profiles of degree of hydration were chosen for the selection of the interface zones length instead. The degree of hydration was observed to be the lowest at the position 0 for all interface zones, namely 0.68, 0.70 and 0.42 for IZ-I, -II and -III, respectively. The IZ limit was chosen as the point where a plateau is reached in the degree of hydration profile. Thus, the IZ thicknesses were estimated as 110 µm,

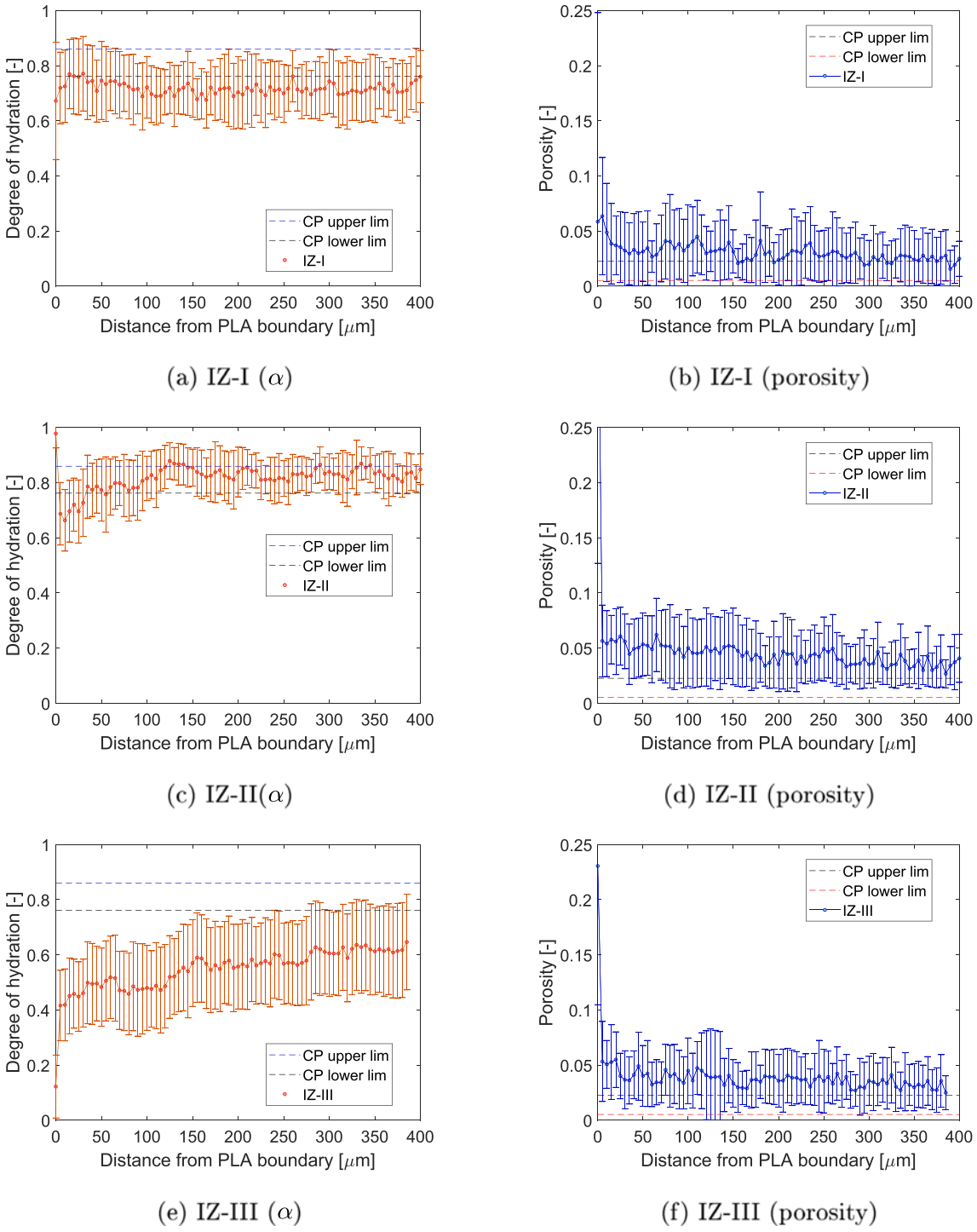

Fig. 6. Degree of hydration profiles from PLA boundary of the IZ of SH-I a), -II c) and -III e) and porosity profiles from PLA boundary of the IZ of SH-I b), -II d) and -III f). The error bars represent the standard deviation among the different micrographs for each position.

130 μm and 260 μm for IZ-I, -II and -III, respectively. These sizes are quite larger than typical mechanical interfaces forming around inert additions such as regular aggregates [50] and even those in overlay systems and around recycled aggregates [25,51]. The values of the degree of hydration beyond the IZ were similar to those in bulk CP (α_{ave} = 0.82) for SH-I and -II, whereas for SH-III there seems to be a more widespread modification of the paste with values of α beyond the IZ of around 0.60.

4.2.2. Elemental analysis

In the bar graph reported in Fig. 7a, the average elemental atomic concentrations, normalized to the calcium concentration, are shown for each studied interface and their respective bulk pastes.

The most striking feature observed in Fig. 7a is the highly heterogeneous nature of SH-III CSH composition. Furthermore, negligible differences were spotted between interface zone and bulk paste of SH-III. The latter confirms the hypothesis formulated in the previous section regarding the more widespread interference in hydration of PLA-III. Traces of phosphorus were detected in both interface and bulk paste

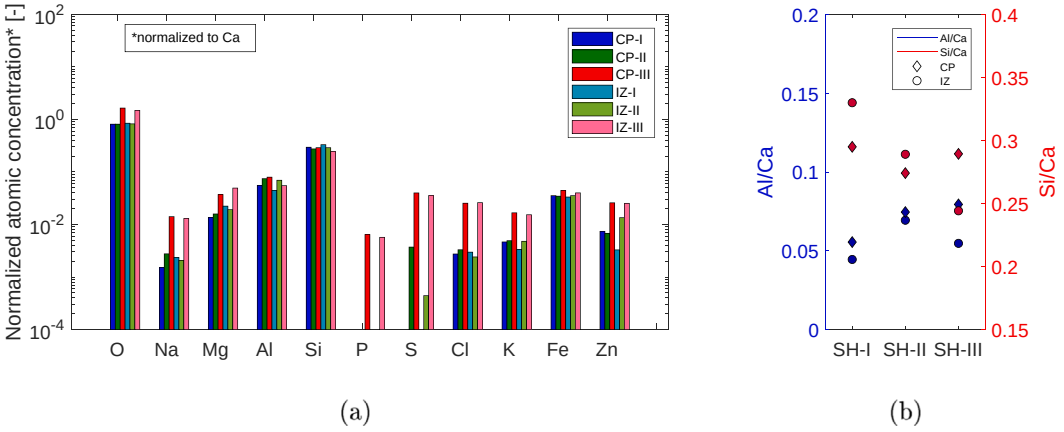

Fig. 7. General elemental atomic compositions a) and aluminum and silica atomic fractions b) normalized to Ca atomic ratio for the interfaces SH-I, SH-II and SH-III and bulk cement paste beyond the IZ, CP-I, -II and -III.

of SH-III, whereas none were detected for SH-I or SH-II. The presence of phosphates in portland cement has been proven to retard hydration and to cause long-term decrements of compressive strength [52,53] which could explain the retardation of early reaction in SH-III and long term lack in hydration degree. Sulfur was also found in relatively high concentrations for interface and bulk paste of SH-III. Smaller concentrations were found for SH-II, specially so for its interface zone, and none for SH-I. Considerably higher concentrations of Cl and alkalis Na and K were detected in SH-III when compared to the references and interfaces of SH-I and SH-II.

Since Ca, Al and Si make the bulk of hydrates in cement paste, we have also reported Al/Ca and Si/Ca ratios in Fig. 7b relative to the interfaces and respective reference bulk pastes. With respect to the references, Si/Ca ratio was higher for interfaces I and II which may indicate a slight localized decalcification of the IZ. For IZ-III instead there was a significant decrease in Si/Ca when compared to the three references. Coherently, also Al/Ca was lower for SH-III interface when compared to the reference bulk paste, which may suggest a higher concentration of Ca in the gel at the interface. A slight decrease in Al/Ca ratio was also found for IZ-I, whereas, no changes in Aluminum concentration could be spotted for the IZ-II with respect to bulk cement paste.

4.3. Mechanical properties of cement-PLA interface

4.3.1. 2D mapping of micromechanical properties at the interface zone

In Figs. 8–11, the maps of elastic modulus and hardness, resulting from the grid nanoindentation, are shown for 6 different locations (a-k) per each of the studied pastes SH-I, -II, -III and CP, respectively. The locations of PLA-pastes in Figs. 8–10 are displayed in such a way that the boundary of the PLA particles (not mapped) is at the left of the map. The contour legend of E modulus map captures the whole range of measured values: 0–60 GPa whereas for the hardness maps the color legend was scaled to the range 0–4 GPa.

Since the depth of indentation, chosen for the computation of the elastic modulus and hardness, is relatively high, the resulting values are indicative of a volume of interaction mostly bigger than individual phases in the hydrated cement pastes. For this reason, the individual indentation values do not correspond rigorously to the micromechanical properties of such phases. Nevertheless, as described in Hughes & Trtik [54], high contrast in these properties can be found between anhydrous grains and hydrates, and clearly pores. From literature, typical values of hardness and elastic modulus for clinker are found to be between 3 and 6 GPa and between 60 and 120 GPa [55], respectively. For CSH there exists a further distinction between Low- (LD) and High-Density (HD) CSH with values of H and E ranging between 0.4 and 1 GPa and 18 and 39 GPa, respectively, with increasing values for increasing density of the CSH phase [55]. Similarly, Portlandite (CH) hardness and elastic modulus values range from 1.5 to 2 GPa and from 40 to 50 GPa [55]. Such indications seem to consistently order the phases by values of hardness or elastic modulus as Clinker > CH > HD-CSH > LD-CSH > Pores. And therefore herein, we could also use such indications to roughly describe key features of the different IZ studied.

From the mappings of both elastic modulus and hardness, it can be observed that more extensive blue zones (i.e. indicating lower stiffness) are present in IZ-III, suggesting that the porosity is high and highly connected when compared to the reference CP. IZ-I and -II do not present such large porous areas but rather uniformly distributed smaller defectuous zones. As observed from SEM/BSE analyses, also from the micromechanical mapping, interface zones of the PLA-pastes present lower degrees of hydration when compared to the reference bulk cement paste, as evinced from the presence of more hubs with values of properties close to those of clinker. The latter seems specially true for IZ-III and less so for IZ-I. In general, IZ-II presented higher hardness values of (likely) CSH phases when compared to -I and -III, but similar values to the bulk cement paste. Similar observations can be made regarding the E modulus.

4.3.2. Uniaxial tensile 2D simulations of the interface zone

In Fig. 12 the cracking history of location 1 of IZ-I is reported, overlapped with the mapping of tensile strength assigned to the lattice elements and alone with the respective load versus displacement response in i. In the curve, the same cracking history events have been annotated. First cracking occurred even before reaching the peak, at a load of around 0.06 mN. Such event it is not reported in Fig. 12. The initial cracked elements were not located at the edges. The peak load was only attained when one of the cracked spots got connected to one of the edges (as observed in a)) at approximately 80 μm from the PLA boundary, which is located within the interface zone as measured from SEM/BSE analysis in Section 4.2.1. The next relevant event was the nucleation of another crack in the opposite edge of the mesh (b), this time further away from the particle boundary at circa 120 μm. Both cracks nucleated in zones with low local tensile strengths (in red). Next, the latter crack and then the first crack propagated along the direction perpendicular to the load in turns. The latter propagation required an increase of the applied force in c) since the second crack had encountered local elements with higher strength.

The alternate propagation of one or the other crack could be noticed throughout the whole simulation. After event d), the load necessary to proceed with the cracks propagation was rapidly decreased probably due to the reduction of the bearing sections to less than half of the pristine section. After point f), the bearing section got reduced to one third of original one at the two cracks locations. The second crack

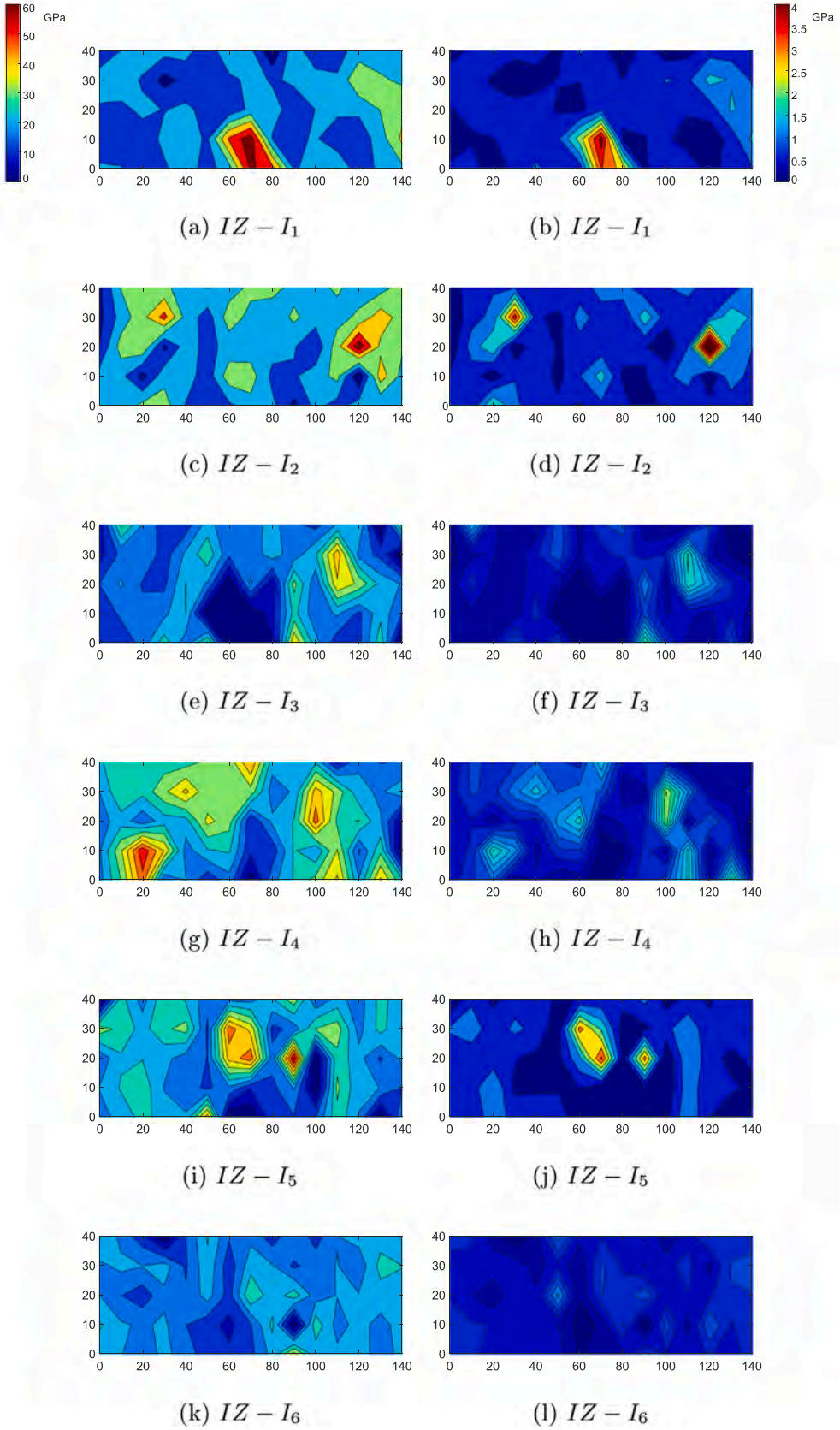

Fig. 8. E modulus (left) and hardness (right) maps obtained from grid nanoindentation for 6 locations at IZ-I.

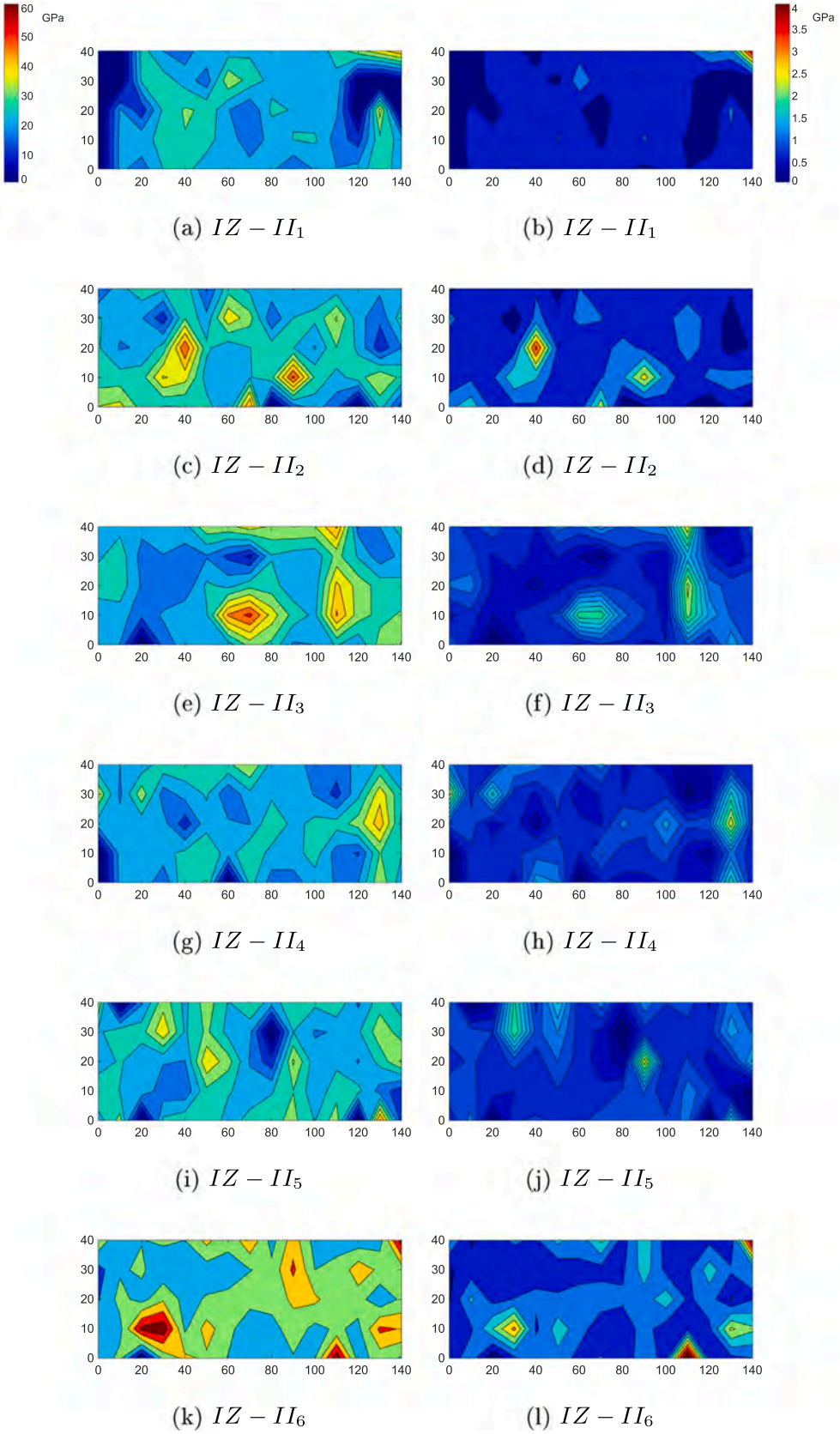

Fig. 9. E modulus (left) and hardness (right) maps obtained from grid nanoindentation for 6 locations at IZ-II.

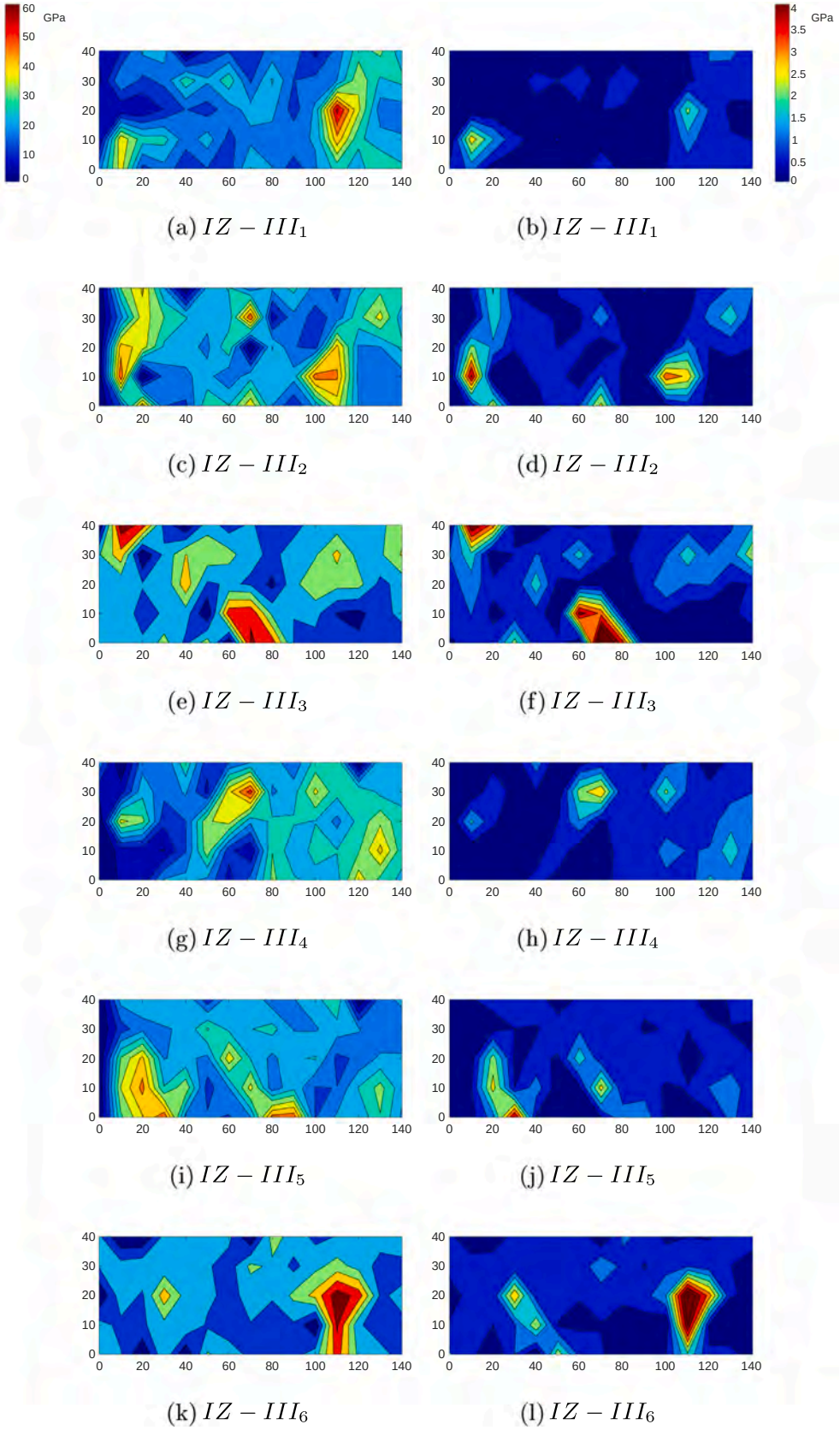

Fig. 10. E modulus (left) and hardness (right) maps obtained from grid nanoindentation for 6 locations at IZ-III.

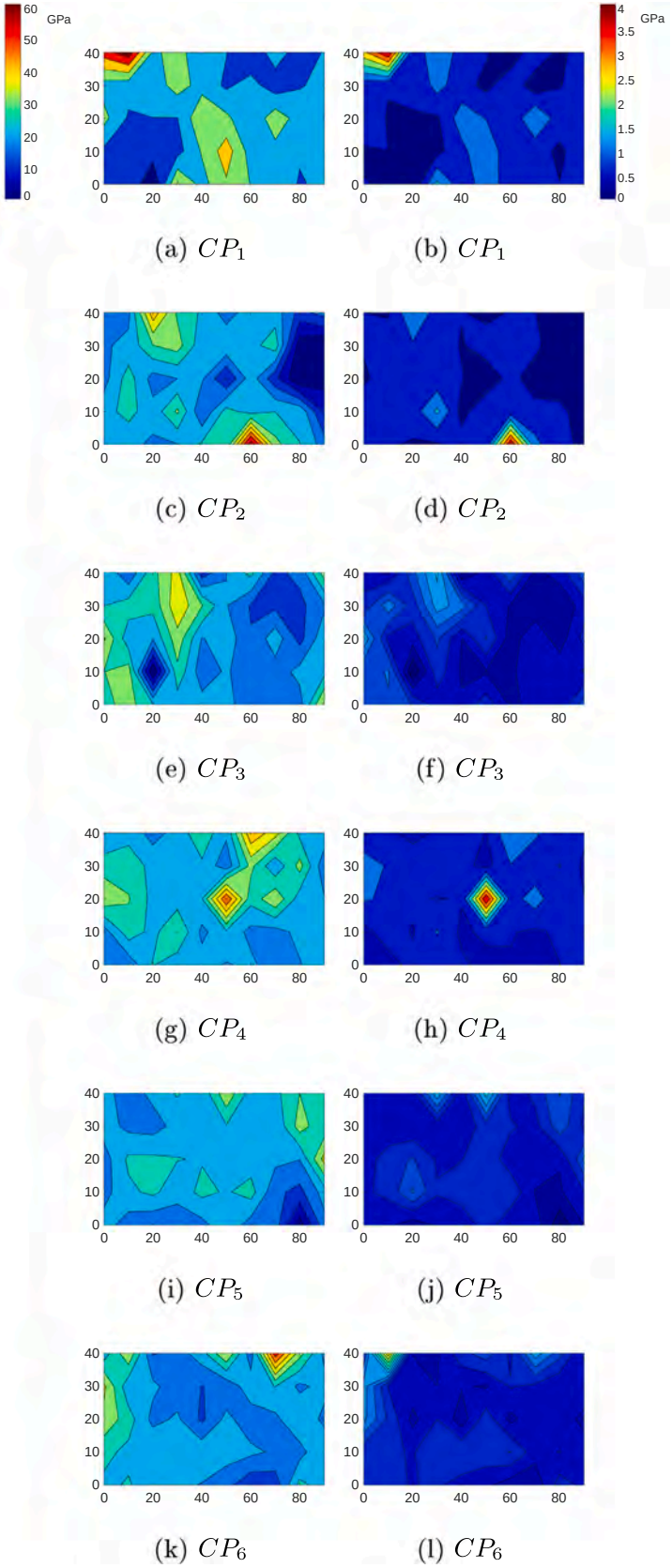

Fig. 11. E modulus (left) and hardness (right) maps obtained from grid nanoindentation for 6 locations in bulk CP.

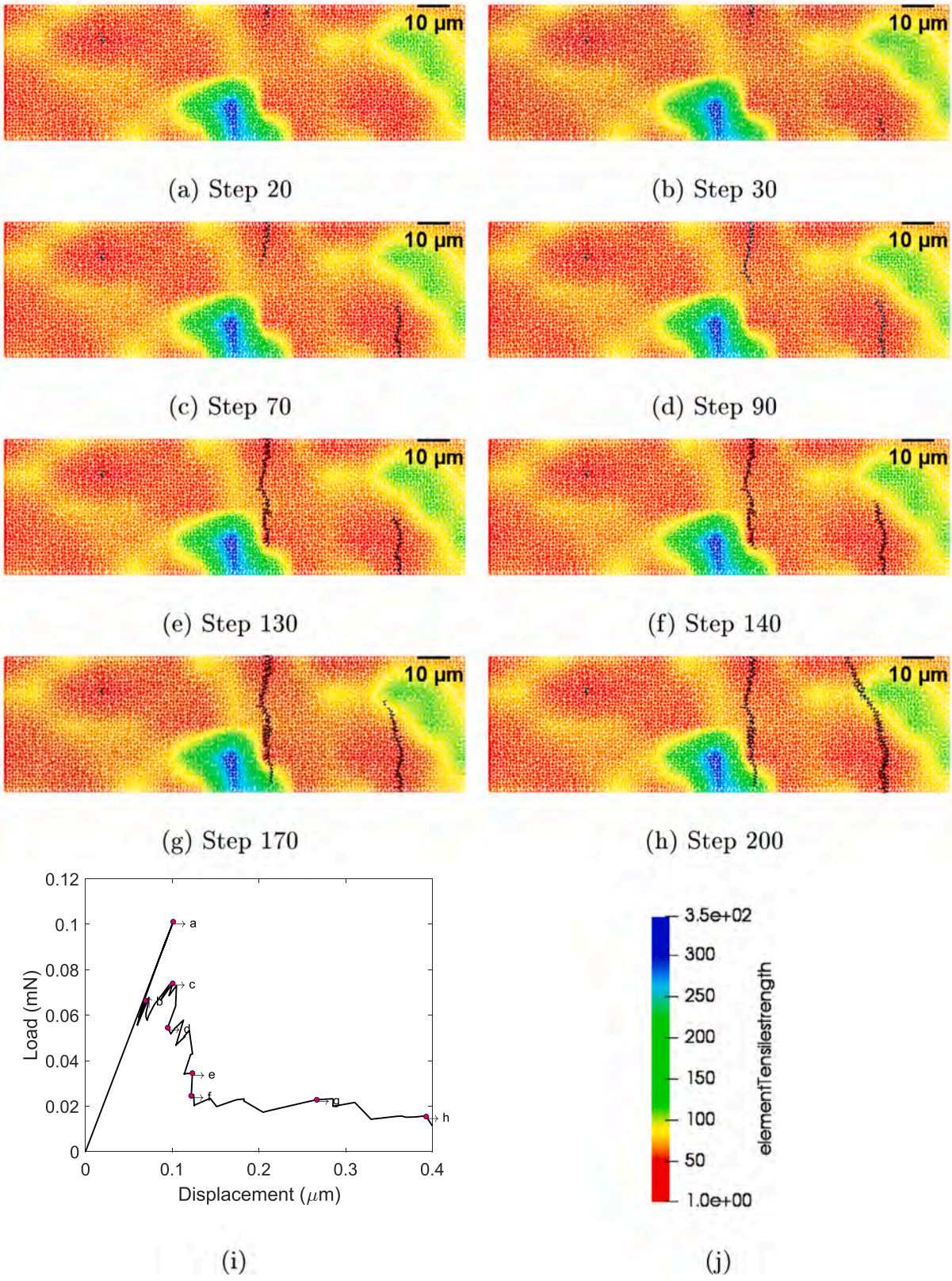

Fig. 12. Cracking history of location 1 of IZ-I (a–h) (cracked elements are reported in black), annotated Load vs. displacement curve (i) and contour color legend (j) of the tensile strength mapping.

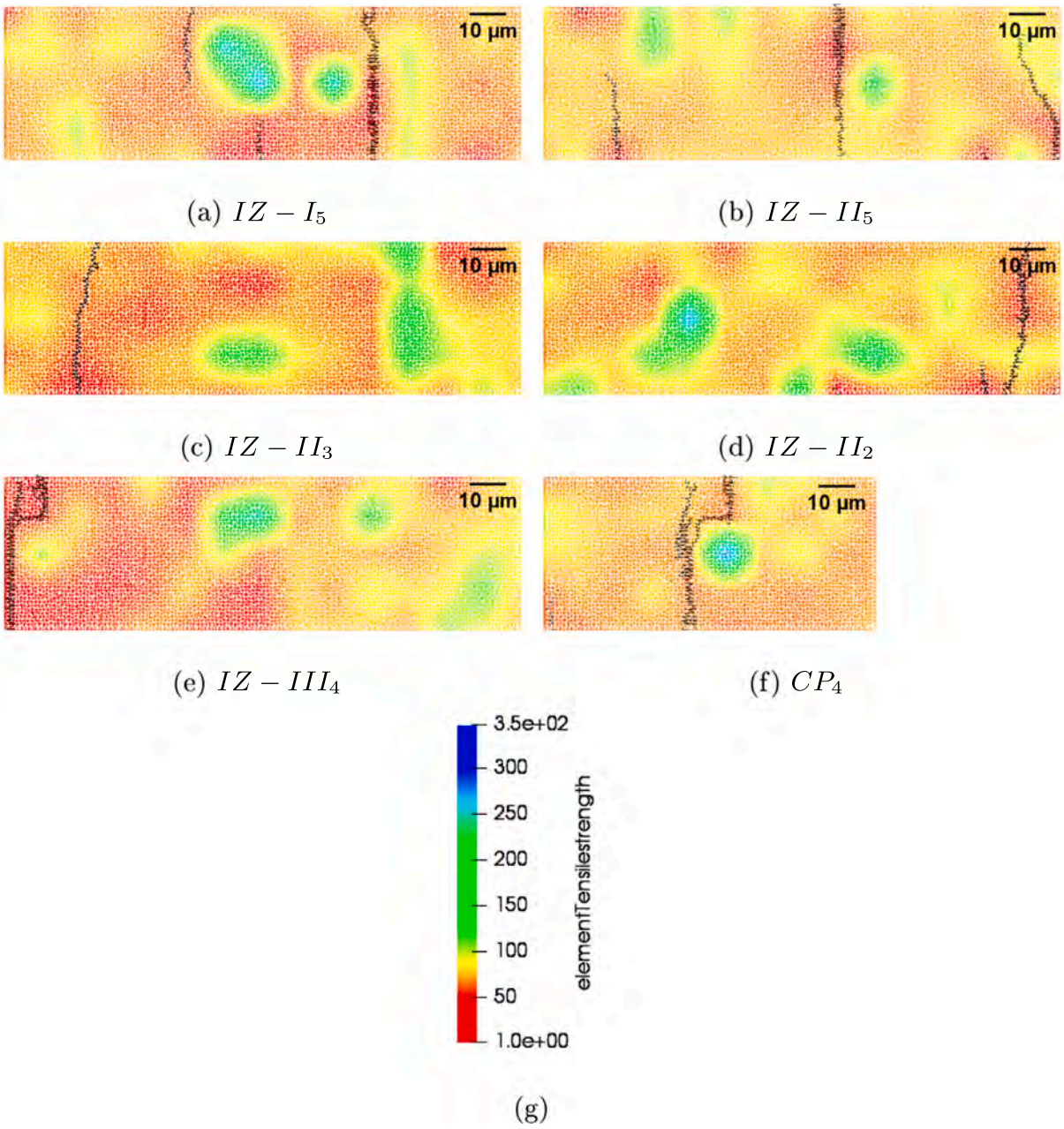

Fig. 13. Common simulated crack patterns at failure of mapped interfaces and bulk cement paste regions.

propagated all the way to the other edge (h) with subsequent lower load due to low local tensile strength near the edge. Since the crack outside of the nominal interface provoked the final failure, the failure was considered to occur in the bulk cement paste and not the interface in this instance.

For the other tested locations, similar developments of cracking events were observed. In Fig. 13, some examples of crack patterns at failure are reported for specific locations from the different simulated pastes. The examples refer to widely observed behaviors of the different interfaces and bulk cement paste. Multiple cracking was observed for several locations of IZ-I and IZ-II, as shown in a) for $IZ - I_5$ and b) for $IZ - II_5$, probably due to the presence of many closely distributed low-tensile-strength hubs from where cracks could easily nucleate, but at the same time the existence of stronger hubs where cracks got trapped during their propagation. Where weaker zones were interconnected, one single crack nucleated and propagated all the way through to the other edge, as was the case reported in c) for $IZ - II_3$. As in the case shown in Fig. 12, in Fig. 13d the other single case of fracture outside of the IZ is reported. In contrast, for IZ-III all locations failed in the IZ and specifically, more failures occurred near the PLA boundary where large weaker zones were commonly present, as shown in e). Finally, the crack pattern at failure of location CP_4 is shown in f). As in the case described in Fig. 12, two cracks nucleated at either side of the section and propagated in turns while diverting around stronger local elements.

The simulated load versus displacement responses of the different tested locations are reported in Fig. 14a–d for CP, IZ-I, -II and -III.

5. Discussion

From each curve in Fig. 14, the tensile strength was calculated as the peak load divided by the area of the section with width of 41 μm and depth of 1 μm (as the cell size). The stiffness of the overall location was considered as equivalent to that of two springs (IZ and bulk cement paste) in series as suggested in [25]. The stiffness of the IZ (E_{IZ}) was

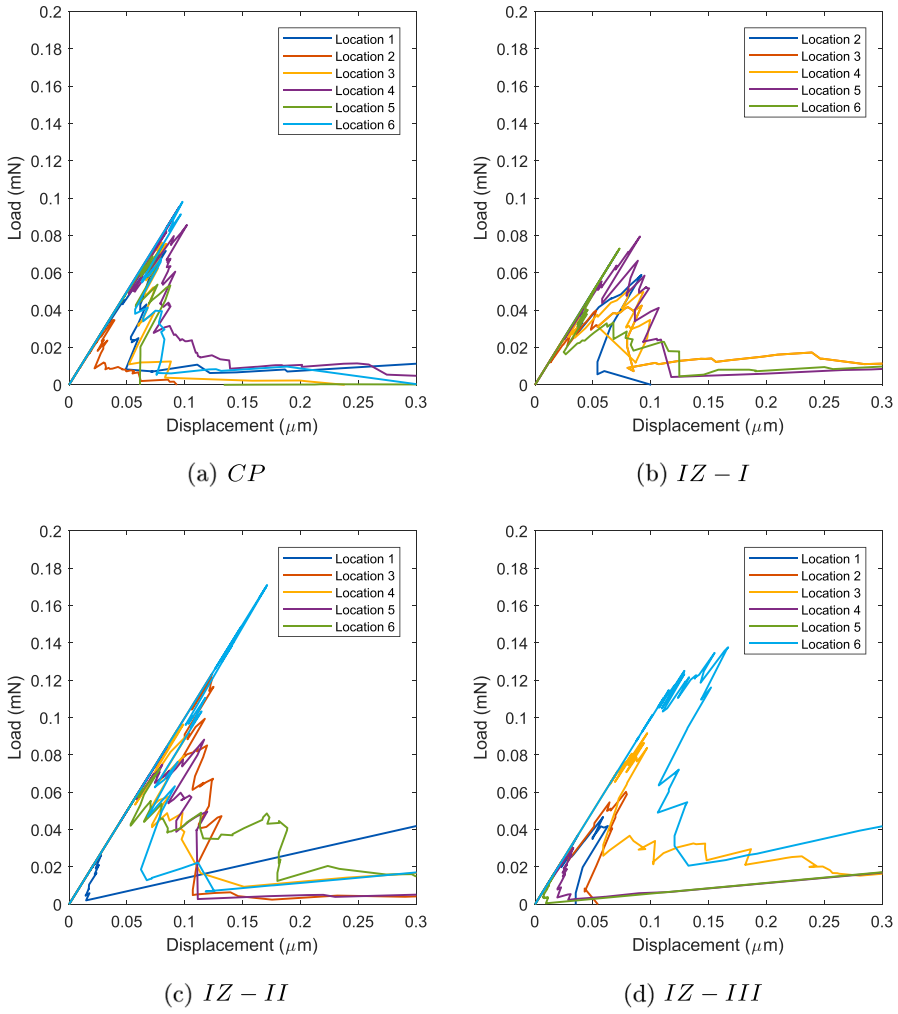

Fig. 14. Simulated load vs. displacement curves for tested locations of bulk cement paste (a) and interfaces (b–d).

calculated considering that the ratio between total area (A_{tot}) and simulated stiffness (E_{tot}) is the sum of the ratio between the area of the IZ (A_{IZ}) and the sought after E_{IZ} and that between the area of the remaining section corresponding to the bulk cement paste ($A_{bulk} = A_{tot} - A_{IZ}$) and the simulated stiffness of the bulk cement paste (E_{CP}) as reported in Equation:

$$\frac{A_{tot}}{E_{tot}} = \frac{A_{IZ}}{E_{IZ}} + \frac{A_{bulk}}{E_{CP}} \tag{5}$$

In Fig. 15 box plots for tensile strength and stiffness of the different interface zones and bulk cement paste are shown. The box plots summarize the samples statistics. The red line inside the boxes is the median

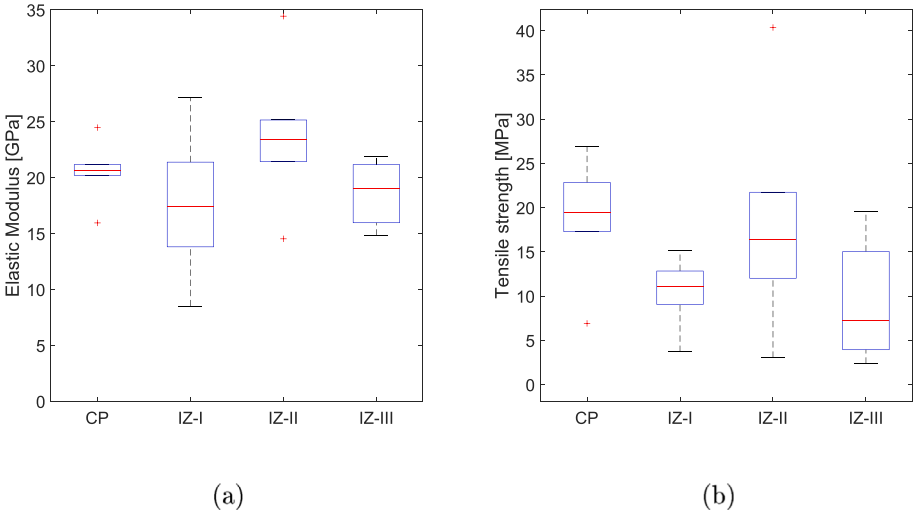

Fig. 15. Summary of stiffness a) and tensile strength b) values obtained from uniaxial tensile simulations of the tested interface and bulk paste locations.

value and the bottom and top of the boxes are the 25th and 75th percentile values. The outliers are represented by a + sign and the whiskers extend to the lower and upper values not considered as outliers. A value was considered as outlier if it was more than three scaled median absolute deviation (MAD) from the median. The scaled MAD is defined as $c * median(|A - median(A)|)$, where $c = -1/(\sqrt{2} * erfcinv(3/2))$.

First of all, the range of tensile strength values obtained for the reference cement paste (17 – 26 MPa), as well as those of elastic moduli (20 – 22 GPa), are in consonant agreement with those found for similar pastes with water-to-cement ratios between 0.4 and 0.5, hydrated for 28 days [56,57].

Regarding tensile strength of simulated IZ locations, the results point towards a decrease in median values for the interface zones when compared to the reference bulk paste. The ratios between median tensile strength of each interface and that of cement paste were found to be 0.65, 0.89 and 0.38 for IZ-I, -II and -III, respectively. As reported, the effect of PLA type on the mechanical properties of their respective interfaces varied significantly, which suggests that PLA capsules can be tailored to modify the interface and therefore the triggering efficiency and the overall mechanical performance of the self-healing material. The different ratios seem to correlate quite well to the distribution of weaker regions of low hardness (thus high porosity) in the 2D hardness maps obtained from grid nanoindentation (Section 4.3.1). For example, IZ-III maps presented very extensive weak zones, specially near the boundary with the PLA capsule, which could also be confirmed by the low degree of hydration in the interface zone of SH-III as observed from BSE analysis. The microstructure of this interface can be explained by the modifications in hydration brought in by the capsules PLA-III, such as dramatic delays of hydration at early age, as shown from the heat flow curves. These microstructural features explain also the positive skewness of the distribution of tensile strength for IZ-III, which emphasizes the greater likelihood of obtaining lower values of strength. In contrast, the other interfaces IZ-I and -II, as well as the CP, presented seemingly normal distributions of tensile strength. Hardness maps of CP, IZ-I and -II showed smaller and well-distributed weak hubs, specially so for IZ-II, which coincided with higher median tensile strength with respect to IZ-III. Decreases in alumina content were also observed in the interfaces IZ-I and IZ-III. From the interquartile ranges of the box plots, it is also possible to notice that both IZ-II and IZ-III tensile strength distributions presented more data dispersion than CP and IZ-I which may be related to the increase of heterogeneity in these interfaces. A similar observation could be made about the higher scatter of the tensile strength values for IZ-II and -III, as denoted from the separation of the whiskers in the plot.

Concerning the stiffness of the simulated locations, median values were in a narrow range, between 17 and 24 GPa, which denotes a weak influence of the PLA particles on the elastic response of their respective interfaces. This is coherent with established research [57] stating that elastic modulus is much more dependent on the continuity of the solid phases rather than on the presence of porosity. The latter seems to be considerably different among the interfaces and bulk cement paste as shown in the hardness and E modulus mapping. Yet, variation on the median values of stiffness was observed. As CP, all the interfaces presented normal distribution of the elastic moduli. When comparing the median values of elastic modulus among the different location types, it is noticeable that IZ-I presented the lowest stiffness, followed by IZ-III and IZ-II, respectively. Decalcification in IZ-I CSH, as seen from EDS point analysis, may have been the cause of the loss of stiffness in the interface phase as it has been reported in [58]. In contrast, no decalcification was observed at the interface II and even an increase in calcium content was identified for IZ-III. The latter may have been negatively compensated by the presence of large zones with low stiffness present at the IZ-III which disrupts the continuity of the solid phases. Notwithstanding, it cannot be ruled out that different types of PLA may change the proportions of HD-CSH and LD-CSH, which can be also responsible for differences in stiffness of the interface with respect to the reference bulk paste. In general, data dispersion and scatter of simulated stiffness were greater for interface locations when compared to bulk CP. The increased variability of both stiffness and tensile strength values for interfaces suggests that although these zones are definitely affected chemically, physically and mechanically, there is higher heterogeneity than in the bulk paste and therefore, their mechanical properties are more variable.

6. Conclusions

In this study, we quantified the tensile strength and elastic modulus of the interface zone (IZ) between bacteria-embedded PLA capsules and cement paste, for their eventual use as input for mesoscale simulations of the self-healing concrete. In order to do so, mapping of the elastic modulus and hardness of the IZ around different types of PLA capsules, embedded in cement paste, and of the bulk unaffected reference cement paste was done through grid nanoindentation. The outcome was then used to simulate uniaxial tensile tests on several data sets through lattice fracture model. Moreover, Scanning Electron Microscopy in Backscattering Electron mode (SEM/BSE) was performed to study the hydrates assemblage distribution around the PLA particles and therefore to determine the extension of the IZ zone. Chemical analysis was performed through EDS to identify differences in elemental composition at the interfaces. The following conclusions can be drawn from the results presented herein:

- The studied PLA capsules interfere with reaction kinetics in the first 120 h of hydration of cement paste. The influence of the additive varies in magnitude in accordance to particle morphology and (alleged) different production processes.
- PLA capsules used in this study definitely modify the long-term hydration of cement paste in the vicinity of the capsules as evinced from the extensive interface zones inferred from the degree of hydration profiles measured through image analysis of BSE images. Mechanical interfaces are typically smaller than 40 μm as reported in literature [50], whereas in this study interfaces for different reactivity grades of PLA were found to range between 110 and 260 μm.
- Porosity profiles along the interfaces, as measured from BSE images, yielded no definitive trend. On the other hand, from grid nanoindentation results, differences were observed in terms of amount of low stiffness indents, between different zones of the grid themselves and between the IZ and the bulk.
- Traces of phosphorus were found via EDS point analysis in the interface zone and bulk paste of certain PLA type contained in cement paste. This correlated to dramatic short and long term hydration hindrance in the cementitious paste, with consequent worsened mechanical properties.
- Grid nanoindentation could provide a qualitative comparison among the degrees of hydration of the different interfaces, via characteristically high values of hardness and elastic moduli of anhydrous phases.
- The ratios between the tensile strength of the PLA interface zones and the bulk cement paste resulted 0.65, 0.89 and 0.38 for SH-I, SH-II and SH-III respectively. These results suggest that PLA can be tailored to optimize the physico-mechanical properties of the interface and hence, the mechanical behavior of the SH system.
- Average values of stiffness for the interface zone of SH-II and SH-III were close to those of unaffected cement paste. The interface IZ-I showed significantly reduced stiffness which seemed to correlate with decalcification of the interface locations as observed from EDS analysis.

Various limitations of the methodology employed here are to be taken into account when interpreting and using the results of this study. One important matter is to consider that on selecting the indented

locations, uncracked areas were preferred, therefore the effect of bigger defects in the interface could not be reflected on the statistics of simulated mechanical properties. Regarding the numerical simulations, it has been shown in literature [34] that elastic moduli and tensile strengths obtained from 2D lattice fracture simulations are consistent with those found for 3D cases. Nonetheless, the distribution of 2D strength was found to be askew towards values up to 30 % higher then their 3D counterpart, which may suggest that the 2D analyses overestimate this property. Notwithstanding, the ratio between this property in bulk cement paste and interfaces should not be affected, as shown in other researches [59].

In the near future the results obtained herein, i.e. ratios between properties of the interface and bulk paste, are to be used as input for fracture simulations at the mesoscale of the self-healing concrete. Phases such as capsules, interface and bulk cement paste will be included to elucidate the effect of the inclusions on mechanical behavior of the composite. We expect that mesoscale fracture modeling will allow to optimize the self-healing material in terms of capsule characteristics, dosage, and other important aspects for the development of such materials.

CRediT authorship contribution statement

C. Romero Rodríguez: Conceptualization, Methodology, Software, Formal analysis, Investigation, Writing - original draft, Visualization. **F. França de Mendonça Filho:** Conceptualization, Methodology, Formal analysis, Investigation, Writing - review & editing. **L. Mercuri:** Methodology, Formal analysis, Investigation, Writing - review & editing. **Y. Gan:** Methodology, Investigation, Writing - review & editing. **E. Rossi:** Methodology, Investigation, Writing - review & editing. **G. Anglani:** Methodology, Investigation, Writing - review & editing. **P. Antonaci:** Resources, Supervision, Writing - review & editing. **E. Schlangen:** Software, Resources, Writing - review & editing, Supervision, Funding acquisition. **B. Šavija:** Methodology, Software, Writing - review & editing, Supervision.

Declaration of competing interest

The authors declare that they have no known competing financial interests or personal relationships that could have appeared to influence the work reported in this paper.

Acknowledgements

The first author acknowledges the financial support from the Construction Technology Research Program funded by the Ministry of Land, Infrastructure and Transport of the Korean Government under the grant 17SCIP-B103706-03. Y. Gan acknowledges the financial support of China Scholarship Council, under grant number 201706130140. We thank Rene Mors from Basilisk for supplying the capsules and for useful suggestions. The authors acknowledge the help of Durga P. Mainali with the SEM microscopy.

References

[1] Z. Li, L.R.d. Souza, C. Litina, A.E. Markaki, A. Al-Tabbaa, Feasibility of using 3d printed polyvinyl alcohol (pva) for creating self-healing vascular tunnels in cement system, Materials 12 (23) (2019) 3872.
[2] L. Mercuri, C. Romero Rodriguez, Y. Xu, S. Chaves Figueiredo, R. Mors, E. Rossi, G. Anglani, P. Antonaci, B. Šavija, E. Schlangen, On the role of soft inclusions on the fracture behaviour of cement paste, Proceedings of the 10th International Conference on Fracture Mechanics of Concrete and Concrete Structures, 2019.
[3] W. Li, Z. Jiang, Z. Yang, H. Yu, Effective mechanical properties of self-healing cement matrices with microcapsules, Mater. Des. 95 (2016) 422–430.
[4] T. Van Mullem, G. Anglani, M. Dudek, H. Vanoutrive, G. Bumanis, C. Litina, A. Kwiecień, A. Al-Tabbaa, D. Bajare, T. Stryszewska, et al., Addressing the need for standardization of test methods for self-healing concrete: an inter-laboratory study on concrete with macrocapsules, Sci. Technol. Adv. Mater..
[5] C. Romero Rodriguez, S. Chaves Figueiredo, B. Chiaia, E. Schlangen, Induction healing of concrete reinforced by bitumen-coated steel fibres, 9th International Conference on Fracture Mechanics of Concrete and Concrete Structures, 2016.
[6] N. De Belie, E. Gruyaert, A. Al-Tabbaa, P. Antonaci, C. Baera, D. Bajare, A. Darquennes, R. Davies, L. Ferrara, T. Jefferson, et al., A review of self-healing concrete for damage management of structures, Adv. Mater. Interfaces 5 (17) (2018) 1800074.
[7] T. Qureshi, A. Kanellopoulos, A. Al-Tabbaa, Encapsulation of expansive powder minerals within a concentric glass capsule system for self-healing concrete, Constr. Build. Mater. 121 (2016) 629–643.
[8] G. Anglani, J.-M. Tulliani, P. Antonaci, Behaviour of pre-cracked self-healing cementitious materials under static and cyclic loading, Materials 13 (5) (2020) 1149.
[9] L. Lv, E. Schlangen, Z. Yang, F. Xing, Micromechanical properties of a new polymeric microcapsule for self-healing cementitious materials, Materials 9 (12) (2016) 1025.
[10] G. Anglani, T. Van Mullem, X. Zhu, J. Wang, P. Antonaci, N. De Belie, J.-M. Tulliani, K. Van Tittelboom, Sealing efficiency of cement-based materials containing extruded cementitious capsules, Constr. Build. Mater. 251 (2020) 119039.
[11] G. Anglani, P. Antonaci, J.-M. Tulliani, K. Van Tittelboom, J. Wang, N. De Belie, Self-healing efficiency of cement-based materials containing extruded cementitious hollow tubes filled with bacterial healing agent, Final Conference of RILEM TC 253-MCI: Microorganisms-Cementitious Materials Interactions, vol. 2, RILEM Publications, 2018, pp. 425–431.
[12] D. Palin, V. Wiktor, H. Jonkers, A bacteria-based bead for possible self-healing marine concrete applications, Smart Mater. Struct. 25 (8) (2016) 084008.
[13] J. Wang, K. Van Tittelboom, N. De Belie, W. Verstraete, Use of silica gel or polyurethane immobilized bacteria for self-healing concrete, Constr. Build. Mater. 26 (1) (2012) 532–540.
[14] J.-Y. Wang, N. De Belie, W. Verstraete, Diatomaceous earth as a protective vehicle for bacteria applied for self-healing concrete, J. Ind. Microbiol. Biotechnol. 39 (4) (2012) 567–577.
[15] V. Wiktor, H.M. Jonkers, Quantification of crack-healing in novel bacteria-based self-healing concrete, Cem. Concr. Compos. 33 (7) (2011) 763–770.
[16] J. Wang, H. Soens, W. Verstraete, N. De Belie, Self-healing concrete by use of microencapsulated bacterial spores, Cem. Concr. Res. 56 (2014) 139–152.
[17] R. Mors, H. Jonkers, Feasibility of lactate derivative based agent as additive for concrete for regain of crack water tightness by bacterial metabolism, Ind. Crop. Prod. 106 (2017) 97–104.
[18] R. Mors, H. Jonkers, Effect on concrete surface water absorption upon addition of lactate derived agent, Coatings 7 (4) (2017) 51.
[19] B. Hilloulin, K. Van Tittelboom, E. Gruyaert, N. De Belie, A. Loukili, Design of polymeric capsules for self-healing concrete, Cem. Concr. Compos. 55 (2015) 298–307.
[20] L.-Y. Lv, H. Zhang, E. Schlangen, Z. Yang, F. Xing, Experimental and numerical study of crack behaviour for capsule-based self-healing cementitious materials, Constr. Build. Mater. 156 (2017) 219–229.
[21] B. Šavija, J. Feiteira, M. Araújo, S. Chatrabhuti, J.-M. Raquez, K. Van Tittelboom, E. Gruyaert, N. De Belie, E. Schlangen, Simulation-aided design of tubular polymeric capsules for self-healing concrete, Materials 10 (1) (2017) 10.
[22] L.M. Mauludin, X. Zhuang, T. Rabczuk, Computational modeling of fracture in encapsulation-based self-healing concrete using cohesive elements, Compos. Struct. 196 (2018) 63–75.
[23] S.V. Zemskov, H.M. Jonkers, F.J. Vermolen, Two analytical models for the probability characteristics of a crack hitting encapsulated particles: application to self-healing materials, Comput. Mater. Sci. 50 (12) (2011) 3323–3333.
[24] E. Tziviloglou, Z. Pan, H.M. Jonkers, E. Schlangen, Bio-based self-healing mortar: an experimental and numerical study, J. Adv. Concr. Technol. 15 (9) (2017) 536–543.
[25] M. Luković, B. Šavija, H. Dong, E. Schlangen, G. Ye, Micromechanical study of the interface properties in concrete repair systems, J. Adv. Concr. Technol. 12 (9) (2014) 320–339.
[26] B. self healing concrete, Material safety data sheet concrete healing agent pla based (cha-pla), https://www.basiliskconcrete.com/wp-content/uploads/2019/12/20181019_HA_MSDS_Material-Safety-Data-Sheet.pdf, (2018).
[27] T. Allen, Particle Size Measurement, Springer, 2013.
[28] M. Megalla, Bacteria Based Self-healing Concrete, Master's thesis, Delft University of Technology, the Netherlands, (2017).
[29] W.C. Oliver, G.M. Pharr, Measurement of hardness and elastic modulus by instrumented indentation: advances in understanding and refinements to methodology, J. Mater. Res. 19 (1) (2004) 3–20.
[30] J. Schindelin, I. Arganda-Carreras, E. Frise, V. Kaynig, M. Longair, T. Pietzsch, S. Preibisch, C. Rueden, S. Saalfeld, B. Schmid, et al., Fiji: an open-source platform for biological-image analysis, Nat. Methods 9 (7) (2012) 676–682.
[31] I. Arganda-Carreras, V. Kaynig, C. Rueden, K.W. Eliceiri, J. Schindelin, A. Cardona, H. Sebastian Seung, Trainable weka segmentation: a machine learning tool for microscopy pixel classification, Bioinformatics 33 (15) (2017) 2424–2426.
[32] N.W. Ritchie, Getting started with nist* dtsa-ii, Microsc. Today 19 (1) (2011) 26–31.
[33] M. Vandamme, F.-J. Ulm, P. Fonollosa, Nanogranular packing of c–s–h at substochiometric conditions, Cem. Concr. Res. 40 (1) (2010) 14–26.
[34] M. Luković, E. Schlangen, G. Ye, Combined experimental and numerical study of fracture behaviour of cement paste at the microlevel, Cem. Concr. Res. 73 (2015) 123–135.
[35] B. Šavija, H. Zhang, E. Schlangen, Micromechanical testing and modelling of blast furnace slag cement pastes, Constr. Build. Mater. 239 (2020) 117841.
[36] E. Schlangen, J. Van Mier, Experimental and numerical analysis of micromechanisms of fracture of cement-based composites, Cem. Concr. Compos. 14 (2) (1992) 105–118.

[37] G. Lilliu, J.G. van Mier, 3d lattice type fracture model for concrete, Eng. Fract. Mech. 70 (7–8) (2003) 927–941.
[38] E. Schlangen, Z. Qian, 3d modeling of fracture in cement-based materials, J. Multiscale Model. 1 (02) (2009) 245–261.
[39] H. Zhang, Y. Xu, Y. Gan, E. Schlangen, B. Šavija, Experimentally validated meso-scale fracture modelling of mortar using output from micromechanical models, Cem. Concr. Compos. (2020) 103567.
[40] Z. Qian, Multiscale Modeling of Fracture Processes in Cementitious Materials, (2012).
[41] M. Hlobil, V. Šmilauer, G. Chanvillard, Micromechanical multiscale fracture model for compressive strength of blended cement pastes, Cem. Concr. Res. 83 (2016) 188–202.
[42] H. Zhang, B. Šavija, S. Chaves Figueiredo, M. Lukovic, E. Schlangen, Microscale testing and modelling of cement paste as basis for multi-scale modelling, Materials 9 (11) (2016) 907.
[43] H. Zhang, Y. Xu, Y. Gan, Z. Chang, E. Schlangen, B. Šavija, Combined experimental and numerical study of uniaxial compression failure of hardened cement paste at micrometre length scale, Cem. Concr. Res. 126 (2019) 105925.
[44] J. Taplin, Proc. 4th Int. Symp. Chem. Com., NBS Monograph 43, vol. II, (1960), p. 927.
[45] N. Singh, S. Prabha, A. Singh, Effect of lactic acid on the hydration of portland cement, Cem. Concr. Res. 16 (4) (1986) 545–553.
[46] R. Schultz, A discussion of the paper effect of lactic acid on the hydration of portland cement by nb singh, s. prapha singh and ak singh, Cem. Concr. Res. 17 (2) (1987) 365–366.
[47] P. Juilland, E. Gallucci, R. Flatt, K. Scrivener, Dissolution theory applied to the induction period in alite hydration, Cem. Concr. Res. 40 (6) (2010) 831–844.
[48] T.C. Powers, T.L. Brownyard, Studies of the physical properties of hardened portland cement paste, J. Proc. 43 (1946) 101–132.
[49] Standard Test Method for Microscopical Determination of Parameters of the Air-void System in Hardened Concrete, Standard, ASTM, 1998.
[50] D.P. Bentz, P.E. Stutzman, E.J. Garboczi, Experimental and simulation studies of the interfacial zone in concrete, Cem. Concr. Res. 22 (5) (1992) 891–902.
[51] J. Xiao, W. Li, Z. Sun, D.A. Lange, S.P. Shah, Properties of interfacial transition zones in recycled aggregate concrete tested by nanoindentation, Cem. Concr. Compos. 37 (2013) 276–292.
[52] A. Tabikh, F. Miller, The nature of phosphogypsum impurities and their influence on cement hydration, Cem. Concr. Res. 1 (6) (1971) 663–678.
[53] M. Singh, Treating waste phosphogypsum for cement and plaster manufacture, Cem. Concr. Res. 32 (7) (2002) 1033–1038.
[54] J.J. Hughes, P. Trtik, Micro-mechanical properties of cement paste measured by depth-sensing nanoindentation: a preliminary correlation of physical properties with phase type, Mater. Charact. 53 (2–4) (2004) 223–231.
[55] S. Gautham, S. Sasmal, Recent advances in evaluation of intrinsic mechanical properties of cementitious composites using nanoindentation technique, Constr. Build. Mater. 223 (2019) 883–897.
[56] H. Zhang, B. Šavija, E. Schlangen, Towards understanding stochastic fracture performance of cement paste at micro length scale based on numerical simulation, Constr. Build. Mater. 183 (2018) 189–201.
[57] C.-J. Haecker, E. Garboczi, J. Bullard, R. Bohn, Z. Sun, S. Shah, T. Voigt, Modeling the linear elastic properties of portland cement paste, Cem. Concr. Res. 35 (10) (2005) 1948–1960.
[58] G. Constantinides, F.-J. Ulm, The effect of two types of csh on the elasticity of cement-based materials: results from nanoindentation and micromechanical modeling, Cem. Concr. Res. 34 (1) (2004) 67–80.
[59] M. Luković, H. Dong, B. Šavija, E. Schlangen, G. Ye, K. van Breugel, Tailoring strain-hardening cementitious composite repair systems through numerical experimentation, Cem. Concr. Compos. 53 (2014) 200–213.